Compaction-Driven Convection in the Growing Inner Core

K W Lim, R. Deguen, D. Cébron, A. Schulze, M. Mandea

AGU ADVANCING EARTH AND SPACE SCIENCES

Geophysical Research Letters

RESEARCH LETTER
10.1029/2024GL110749

Compaction-Driven Convection in the Growing Inner Core

K. W. Lim[1,2,3], R. Deguen[2], D. Cébron[2], A. Schulze[4], and M. Mandea[1]

[1]CNES – Centre National d'Études Spatiales, Paris, France, [2]Université Grenoble Alpes, Université Savoie Mont Blanc, CNRS, IRD, UGE, ISTerre, Grenoble, France, [3]Now at Université Paris Cité, Institut de Physique du Globe de Paris, CNRS, Paris, France, [4]Heidelberg University, Heidelberg, Germany

Key Points:

- For the first time we simulate inner core growth via compaction and melt migration in spherical geometry (assuming axisymmetry)
- The inner core can develop convective flows under certain parameter ranges to create internal structural heterogeneities
- Assuming values of relevant physical parameters, the Earth's inner core can be expected to exhibit compaction-driven convection today

Supporting Information:

Supporting Information may be found in the online version of this article.

Correspondence to:

K. W. Lim,
kwlim@ipgp.fr

Citation:

Lim, K. W., Deguen, R., Cébron, D., Schulze, A., & Mandea, M. (2024). Compaction-driven convection in the growing inner core. *Geophysical Research Letters*, *51*, e2024GL110749. https://doi.org/10.1029/2024GL110749

Received 13 JUN 2024
Accepted 15 NOV 2024

Abstract The Earth's inner core (IC) is known to exhibit heterogeneous structures with their origins still unknown. From the onset of nucleation, the IC can grow via sedimentation and compaction of iron crystals freezing out from the fluid outer core. Previous studies of IC growth have shown entrapment of fluid within the solid matrix, and unstable density profiles in 1D can appear depending on the efficiency of fluid percolation. In this study, we perform simulations of IC growth in spherical geometries (assuming axisymmetry). We find that it is possible for the IC to develop large-scale convective flows under certain conditions and, in some instances, produce small-scale heterogeneites close to the IC boundary. Assuming representative values for the physical properties of the Earth's IC, we show that it is possible for the IC to exhibit compaction-driven convection today.

Plain Language Summary The Earth's inner core is a solid body composed primarily of an iron-nickel alloy, formed from crystallization of the fluid outer core over time. Seismologists studying its structure have found some peculiarities such as elastic properties that depend on direction, but figuring out the cause of these peculiarities have been challenging. One theory is the presence of fluids trapped within the solid body of the inner core during its growth, giving rise to its anomalous structure and seismic velocities. In this study, we model the growth of the inner core in 3D spherical geometry (assuming cylindrical symmetry) to investigate the distribution of fluids in the interior. We observe that under certain conditions, instabilities can develop across different scales in the interior which redistribute the fluids within. Taking certain representative values of the properties of the Earth's core, it is possible that instabilities are present in the inner core today.

1. Introduction

The growth of Earth's inner core is inextricably linked to the thermal and compositional evolution of the core (e.g., Breuer et al., 2015; Hirose et al., 2013), thus understanding its origins can provide key insights into the Earth's magnetism and core-mantle boundary (CMB) interactions (Buffett, 2015; J. Hernlund & McNamara, 2015). During Earth's thermal evolution, light elements and latent heat were released as the liquid outer core partially crystallized at the inner core boundary (ICB). This process provided additional energy sources to power the geodynamo, with dynamo simulations showing a marked increase of the core magnetic field strength during inner core nucleation (ICN) (Landeau et al., 2017). Paleomagnetic studies have also suggested that ICN began right after a period of ultralow paleointensities recorded in the Ediacaran (e.g., Bono et al., 2019; Shcherbakova et al., 2020; Thallner et al., 2021), implying that the inner core age is ∼0.5 Ga. Thermal evolution models of the core using values of thermal conductivity around 100 W m^{-1} K^{-1} have also shown preference for a later nucleation onset time (e.g., Driscoll, 2016; Labrosse, 2015).

Several seismology studies and reviews of inner core structure have discussed heterogeneities and anisotropy across different scales (Deuss, 2014; Souriau & Calvet, 2015; Sumita & Bergman, 2015; Tkalčić et al., 2022; Waszek et al., 2023). For instance, analyses of P-wave data have revealed a faster component in the polar direction compared to the equatorial direction (e.g., Morelli et al., 1986; Poupinet et al., 1983; Song & Helmberger, 1993; Woodhouse et al., 1986). Coupled with the observed high attenuation structure (Andrews et al., 2006; Cao & Romanowicz, 2009; Tkalčić & Phạm, 2018), different hypotheses have been put forth to interpret these observations.

A possible explanation for the observed high attenuation and low S-wave velocities is the presence of melt in the inner core (Singh et al., 2000; Vočadlo, 2007). Prior to ICN, the liquid core is an iron alloy containing some amounts of light elements (Hirose et al., 2013; McDonough, 2014) and as it cooled, the first iron crystals appeared while enriching the liquid in light elements. When and where the first crystals appeared is still unclear because

supercooling could have delayed crystallization (Huguet et al., 2018; Wilson et al., 2021), but regardless of how ICN initiated, the change in light element concentration during core cooling creates a temperature gap between the solidus and liquidus of the core. The coexistence of solid and liquid phases thus creates a mushy inner core. The ICB can be defined as the radius where the outer core's adiabat crosses the iron alloy liquidus, exactly where crystals precipitate to form the inner core (Fearn et al., 1981; Loper & Fearn, 1983; Loper & Roberts, 1981). Presently, there are two proposed mechanisms for melt entrapment close to the ICB: the creation of morphological instabilities from a solidification front (Alexandrov & Malygin, 2011; Deguen et al., 2007; Fearn et al., 1981; Shimizu et al., 2005), and the sedimentation of iron crystals (Gubbins et al., 2008; Lasbleis et al., 2020; Sumita et al., 1996; Wong et al., 2018, 2021). Melts enriched in light elements experience increased buoyancy while the denser crystals undergo compaction due to their weight, thereby expelling melt from the pore spaces. The degree of melt expulsion depends on the solid matrix viscosity and viscous friction between both phases. With less melt remaining in the solid matrix, the efficiency of melt extraction is expected to decrease due to reduced permeability (Faul, 2001). Hence, it is likely that melts were trapped during inner core growth, but the extent and distribution are unconstrained.

The inner core is largely spherical with gravitational acceleration increasing outwards. As the inner core's growth rate decreases with time, compaction of the solid iron matrix is most efficient at the ICB, resulting in a denser, solid-rich region near the ICB. In other words, a gravitationally unstable porosity structure can form within the inner core with larger melt fraction at depths. Previous studies of inner core compaction have shown the existence of such unstable structures (Lasbleis et al., 2020; Sumita et al., 1996) but as these models were in 1D, modeling the development of 2D instabilities was impossible.

In this study, we present new results obtained from simulations that capture the development of instabilities during inner core growth, providing preliminary insights into the 3D interior structure of the inner core and its implications for seismic observations.

2. Methods

To investigate the dynamics of inner core growth in the context of matrix compaction and fluid migration, we adopt the two-phase formulation of Boukaré and Ricard (2017) but excluding the effects of temperature and phase change. As a first step toward a more complete model of inner core dynamics, we neglect the effects of thermal buoyancy and phase change, even though temperature-induced density variations could in principle either drive large-scale convection (if the temperature profile is superadiabatic) or limit radial motion (if subadiabatic), depending on the viscosity, thermal conductivity, and age of the inner core (Lasbleis & Deguen, 2015). In other words, our study assumes that the temperature profile is almost always adiabatic. We solve the equations governing the conservation of mass, momentum, fluid fraction, and the divergence of the "action-reaction" equation (Bercovici et al., 2001) as follows:

$$\nabla \cdot \boldsymbol{v} = 0, \tag{1}$$

$$-\nabla \pi + \nabla \cdot \underline{\boldsymbol{\tau}} - \Delta\rho\phi\boldsymbol{g} = \boldsymbol{0}, \tag{2}$$

$$\frac{\partial \phi}{\partial t} + \nabla \cdot [\phi \boldsymbol{v} - \phi(1-\phi)\boldsymbol{u}] = \epsilon \nabla^2 \phi, \tag{3}$$

$$\nabla \cdot \left\{ \frac{k}{\eta_f} \left[\nabla \pi + \eta_s \nabla \left(\frac{1-\phi}{\phi} D \right) + \Delta\rho \boldsymbol{g} \right] \right\} = D, \tag{4}$$

where $\boldsymbol{v}$ is the volume-averaged velocity, that is, $\boldsymbol{v} = \phi \boldsymbol{v}_f + (1-\phi)\boldsymbol{v}_s$ with the subscripts f and s denoting the fluid and solid components respectively, ϕ is the fluid fraction, $\underline{\boldsymbol{\tau}} = \eta\left[\nabla \boldsymbol{v} + (\nabla \boldsymbol{v})^{\dagger}\right]$ is the viscous stress tensor of the mixture with † denoting the transpose, η is the dynamic (shear) viscosity of the mixture, $\Delta\rho = \rho_s - \rho_f$ is the density difference between both phases, $\boldsymbol{g}$ is the gravity vector, $\nabla\pi = \nabla P - \rho_s \boldsymbol{g}$ (P is the isotropic pressure), $\boldsymbol{u} = \boldsymbol{v}_s - \boldsymbol{v}_f$ is the velocity difference between both phases, $D = \nabla \cdot (\phi \boldsymbol{u})$, ϵ is an artificial diffusivity introduced for numerical stabilization purposes (details in Section 2.2 and Text S2 in Supporting Information S1), k is the permeability which is a function of ϕ, and t is time. In our study, since $\rho_s > \rho_f$, $\Delta\rho$ is strictly positive. Equation 4 is

similar to a Darcy equation that describes the movement of the fluid phase relative to the solid phase which can undergo viscous deformation. As the inner core's permeability is highly unconstrained, we assume a simple permeability law where k is isotropic and varies linearly with ϕ^2, that is, $k = k_0\phi^2$, due to small porosities (e.g., von Bargen & Waff, 1986; Turcotte & Morgan, 1992). The proportionality factor k_0 encompasses properties of the solid matrix such as grain size d and pore geometry K, and we can suppose that $k_0 \propto d^2/K$. Although it is possible for d to be depth dependent from effects such as grain growth (which makes k_0 depth dependent too), we neglect these additional effects and assume k_0 is constant. Lastly, the mixture viscosity in Equation 2 is expected to depend on ϕ such that η varies from η_s when $\phi = 0$ to η_f when $\phi = 1$, but we assume that it is independent of ϕ. We also assume that the mixture is a Newtonian fluid even if both phases are not. While this is a simplification, we expect viscosity variations to be small since ϕ is expected to be small in the inner core.

2.1. Growing Axisymmetric Inner Core

Equations 1–4 are solved in the cylindrical coordinate system with axisymmetric geometry (no azimuthal component and azimuthal variations). To account for the growing inner core and ICB without adjusting the mesh at each time step, we replace the cylindrical coordinates r and z with a nondimensional time-dependent coordinate system $r' = r/R(t)$ and $z' = z/R(t)$ respectively where $R(t)$ is the radius of the inner core at time t. In accordance with previous studies regarding the core's thermal evolution (e.g., Deguen & Cardin, 2011; Labrosse et al., 2001), the ICB evolves according to $R(t) = R_0\sqrt{t/t_0}$, where R_0 and t_0 are the present day inner core radius and age, respectively. Since the coordinates are time-dependent, the Lagrangian time derivative of ϕ needs to include additional terms for the coordinate drift. The transport equation accounting for the changing coordinates due to a growing inner core is therefore:

$$\left.\frac{\partial\phi}{\partial t}\right|_{r'z'} + \nabla\cdot[\phi\boldsymbol{v} - \phi(1-\phi)\boldsymbol{u}] = \epsilon\nabla^2\phi + \frac{\dot{R}}{R}\left(r'\frac{\partial\phi}{\partial r'} + z'\frac{\partial\phi}{\partial z'}\right). \tag{5}$$

In our study, we assume that the gravitational force $\boldsymbol{g}$ grows linearly as a function of distance from the center and that the vector always points toward the center.

2.2. Numerical Approach

With a growing inner core in our model, we chose time dependent velocity- and length-scales where the lengths and velocities $(\boldsymbol{v},\boldsymbol{u})$ are nondimensionalized by the inner core radius $R(t)$ and growth rate $V(t) = \dot{R}(t)$ respectively, time by t_0, pressure by $\eta_s V/R$, and D by V/R. Plugging these into Equations 1, 2, 4 and 5, we obtain the following velocity scales from our nondimensional equations (Text S1 in Supporting Information S1):

$$V_D = \frac{\Delta\rho g_0 k_0}{\eta_f}, \tag{6}$$

$$V_s = \frac{\Delta\rho g_0 R_0^2}{\eta_s}, \tag{7}$$

$$V_0 = \frac{R_0}{2t_0}, \tag{8}$$

where V_D is the Darcy velocity scale associated with the solid-fluid phase velocity difference, V_s is the velocity scale associated with viscous compaction of the solid matrix, and V_0 is the growth rate of the inner core at t_0. From the three velocity scales, we can build two nondimensional numbers V_s' and V_D' that describe the dynamics. Including the dimensionless numerical diffusivity ϵ', we have three nondimensional numbers (Text S1 in Supporting Information S1)

$$V_s' = \frac{V_s}{V_0}, \tag{9}$$

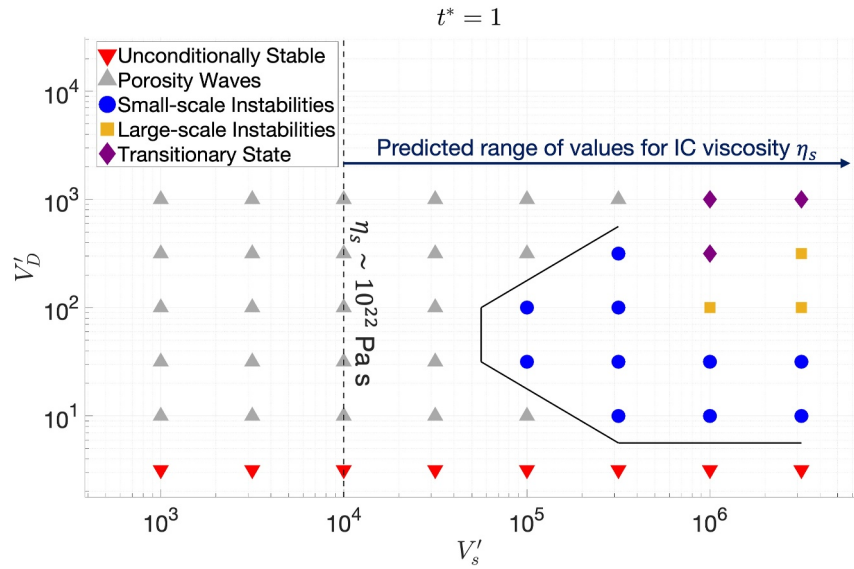

Figure 1. A regime diagram of the simulation results according to the porosity structure at $t^* = 1$ with each symbol representing different regimes. The dashed line shows the minimum possible value of V_s' for $\eta_s \sim 10^{22}$ Pa s while the solid black line shows the transition between 1D and 2D effects.

$$V_D' = \frac{V_D}{V_0}, \tag{10}$$

$$\epsilon' = \frac{\epsilon t_0}{R_0^2}. \tag{11}$$

We use the finite element solver COMSOL Multiphysics® to solve the nondimensional equations in 2D axisymmetric space dimension without a steady azimuthal flow component. Since COMSOL Multiphysics® uses finite element methods, solving convection-dominated transport equations is highly challenging. The transport of ϕ is actually non-diffusive (e.g., Bercovici et al., 2001; McKenzie, 1984), but because mesh-based methods are susceptible to numerical diffusion regardless of the mesh size (see Lee et al., 2024), an artificial diffusive term is included in Equation 3 to obtain control over the degree of diffusion in this problem. Further information about the artificial diffusivity and numerical details of our simulations can be found in Texts S2 and S3 in Supporting Information S1, respectively.

In all our simulations, we apply a (shear) stress free boundary at the ICB

$$\boldsymbol{v} \cdot \boldsymbol{n} = 0, \ \left(\underline{\boldsymbol{\tau}} \cdot \boldsymbol{n}\right) \times \boldsymbol{n} = \boldsymbol{0}, \tag{12}$$

where $\boldsymbol{n}$ is the normal to the ICB. Our boundary conditions are $\phi = \phi_0$, with $\phi_0 = 0.4$, and $D = 0$ at the ICB. The former assumes the liquid fraction at the ICB is close to the disaggregation limit. Above this limit, the solid matrix becomes disconnected and the mixture transitions from a mush to a slurry-like state (Hier-Majumder et al., 2006). The initial conditions are $\phi = \phi_0$ and $D = 0$ everywhere, which is consistent with our boundary conditions.

3. Results

We vary V_s' between 10^3 and $10^{6.5}$ and V_D' between $10^{0.5}$ to 10^3, with every simulation beginning at $t^* = 0$ (the time shortly after ICN) and ending at $t^* = 1$ (the present day), where t^* is the nondimensional time (Text S1 in Supporting Information S1). The results of each simulation can be categorized into five distinct groups according to the characteristics of their 2D porosity profile and velocity fields at $t^* = 1$: (a) unconditionally stable, (b) porosity waves, (c) small-scale instabilities, (d) large-scale instabilities, and (e) transitionary state. They are summarized in the regime diagram (Figure 1) with each regime represented by their own unique symbols and

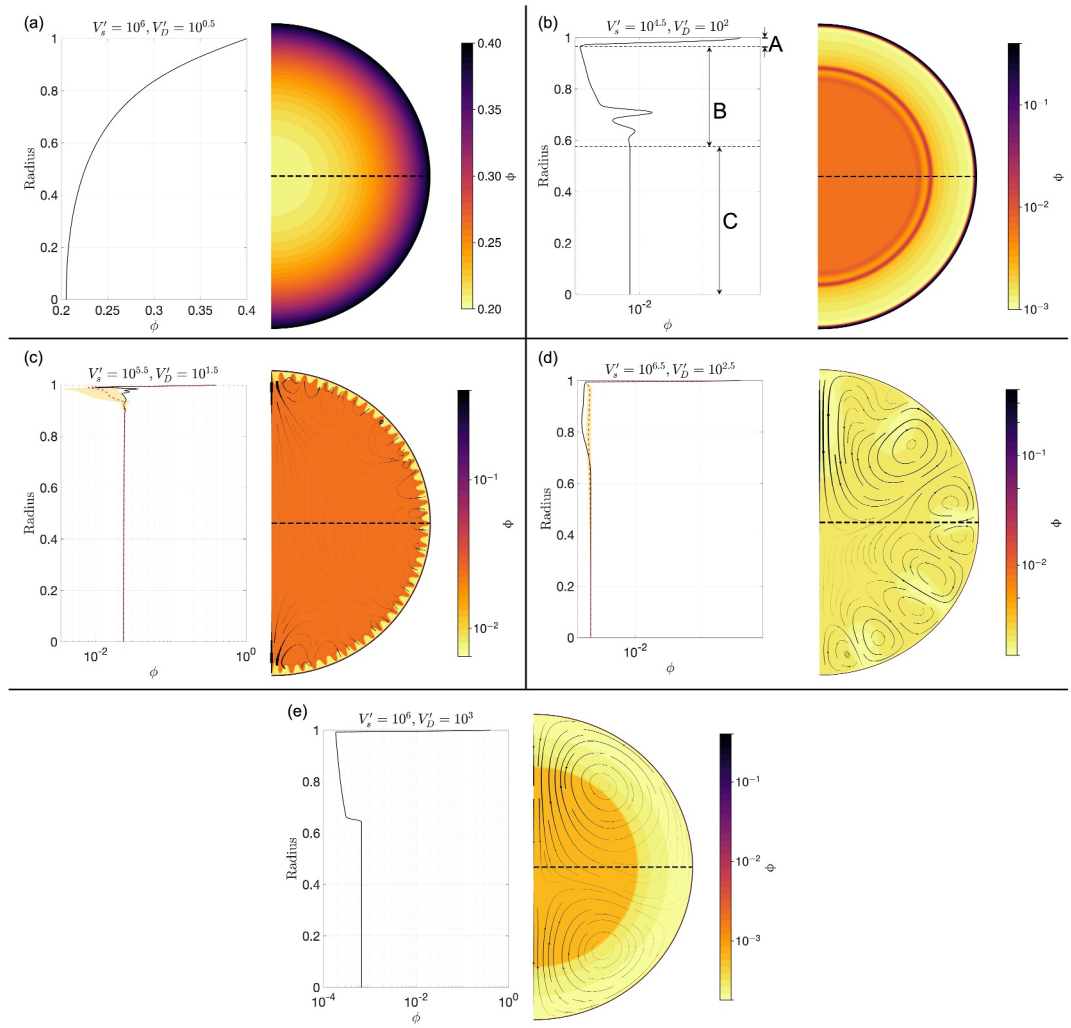

Figure 2. Examples of porosity fields from different regimes. In each sub-figure, the equatorial and latitudinal-averaged porosity profiles are shown on the left halves in black solid and red dashed lines, respectively. The orange bands show the 1σ value from the mean. The right halves show the 2D porosity distribution with colors in log scale. The black dashed lines indicate the equatorial slice while the black lines with arrows in (c)–(e) show the streamlines of $\boldsymbol{v}$ with thickness proportional to $|\boldsymbol{v}|$. (a) Unconditionally stable: $(V_s', V_D') = (10^6, 10^{0.5})$, (b) Porosity waves: $(V_s', V_D') = (10^{4.5}, 10^2)$, (c) Small-scale instabilities: $(V_s', V_D') = (10^{5.5}, 10^{1.5})$, (d) Large-scale instabilities: $(V_s', V_D') = (10^{6.5}, 10^{2.5})$, (e) Transitionary state: $(V_s', V_D') = (10^6, 10^3)$.

colors. We note that the regime diagram actually evolves with time (Figure S1 in Supporting Information S1), but since the present day state is only of interest in this study, we focus our discussions based on Figure 1 and explain our rationale for the categorization in the following sections.

3.1. Unconditionally Stable

We consider an unconditionally stable result when the final porosity profile monotonically decreases from the ICB to the center, corresponding to a stable buoyancy profile (Figure 2a). This regime is represented by red inverted triangles in Figure 1 and occurs in simulations with low V_D' $\left(\sim 10^{0.5}\right)$ regardless of the magnitude of V_s'. In this regime, the small value of V_D' implies relatively weak Darcy flow and thus, inefficient fluid extraction. Hence, even when V_s' is large, Darcy friction is still sufficiently strong to retain significant amounts of fluid in the interior. This reduces radial variations in porosity which also reduces the strength of matrix compaction. In this regime, the entire inner core is dominated by Darcy balance, where Darcy friction is balanced by buoyancy forces (Figure S2 in Supporting Information S1).

3.2. Porosity Waves

The gray triangular symbols represent the departure from the unconditionally stable density profile and, in some cases, the appearance of radial porosity waves. In this regime, the radial porosity profile can be subdivided into three distinct regions (Figure 2b). The outer region A contains the stable boundary layer where ϕ decreases monotonically with depth from ϕ_0 at the ICB to a global minimum $\phi_{\min}$. This porosity structure is a result of the balance between matrix deformation and buoyancy forces, and the decreasing porosity with depth is driven by matrix compaction. It can also be understood that as the inner core grows after ICN, some fraction of liquid is present within the solid matrix, with the largest fraction close to the ICB. Since gravity is the strongest in this region, compaction is most efficient which results in $\phi = \phi_{\min}$ at the base of region A, burying a high liquid fraction beneath. Noting δ as the boundary layer thickness, the viscous deformation and buoyancy forces scale accordingly as $\eta_s V/\delta^2$ and $\Delta\rho g_0 R/R_0$, respectively. Balancing these two terms, we obtain a scaling for the thickness of region A:

$$\delta \sim \frac{R_0}{\sqrt{V_s' t^*}}, \tag{13}$$

similar to Equation 76 from Sumita et al. (1996). In region B, ϕ increases from $\phi_{\min}$ with depth, sometimes accompanied by oscillations from porosity waves, until it approaches a value of ϕ_c. In region C, the porosity approaches ϕ_c toward the center and this is where Darcy balance occurs. Assuming that ϕ_c only varies in time and there is only Darcy balance in this region, it can be shown that ϕ_c depends on V_D' and t^* as follows:

$$\phi_c = \left(\frac{3}{2} V_D' t^* + F\right)^{-1}, \tag{14}$$

where F is an integration constant (Text S4 in Supporting Information S1). The porosity waves in region B are actually fluid-rich layers sandwiched between denser solid-rich layers, with the fluids originating from region C. Percolation induces a net upward flux of fluid from region C to B. However, as permeability is decreasing across B due to decreasing ϕ, fluid percolation becomes increasingly difficult radially outwards. This results in fluid accumulating within region B which further enhances buoyancy variations across this region. These fluid-rich regions subsequently propagate through decompaction at the fluid head and compaction at the tail end in a wave-like manner. The changing force balance is shown in Figure S3 in Supporting Information S1.

The unconditionally stable and porosity waves regimes have spherically symmetric structures associated with ϕ transport dominating in the radial direction. Since a non-zero spherically symmetric velocity field is impossible for $\boldsymbol{v}$ due to Equation 1, this means that ϕ is advected by $-(1-\phi)\boldsymbol{u}$ in Equation 3 (Text S5 in Supporting Information S1) and ΔP only varies in the spherical radial direction (Text S6 in Supporting Information S1). Even though the porosity profiles in this regime are gravitationally unstable, the positive buoyancy of the boundary layer inhibits the deeper layers from overturning. This is further exacerbated by the viscous coupling between regions A and B in our isoviscous model.

3.3. Small-Scale Instabilities

We distinguish simulations of (c) from (b) (defined in the beginning of Section 3) by observing departures from spherical symmetry, even though porosity waves can be considered as small-scale instabilities (e.g., Aharonov et al., 1995; Scott & Stevenson, 1986). The simulations represented by blue circles exhibit small-scale Rayleigh-Taylor instabilities which results in two types of structures observed at $t^* = 1$: a sinusoidal wave-like morphology in the latitudinal direction (Figure 2c) and plume structures originating from below the ICB (Figure S4 in Supporting Information S1). These instabilities typically develop locally along the outermost wavefront of the porosity waves as the buoyancy contrast between this fluid rich layer and the overlying low porosity layer is the largest. The wavelength of these instabilities are approximately of the same order of magnitude as the width of the porosity wave peaks. In this regime, horizontal fluctuations along the interface of these two regions have sufficient torque to generate vorticity, amplifying the fluctuations and driving $\boldsymbol{v}$ to create the observed sinusoidal structures. Eventually, the fluctuations can be sufficiently large to create downwelling plume structures containing solid-rich material (Figure S4 in Supporting Information S1 and Movie S1).

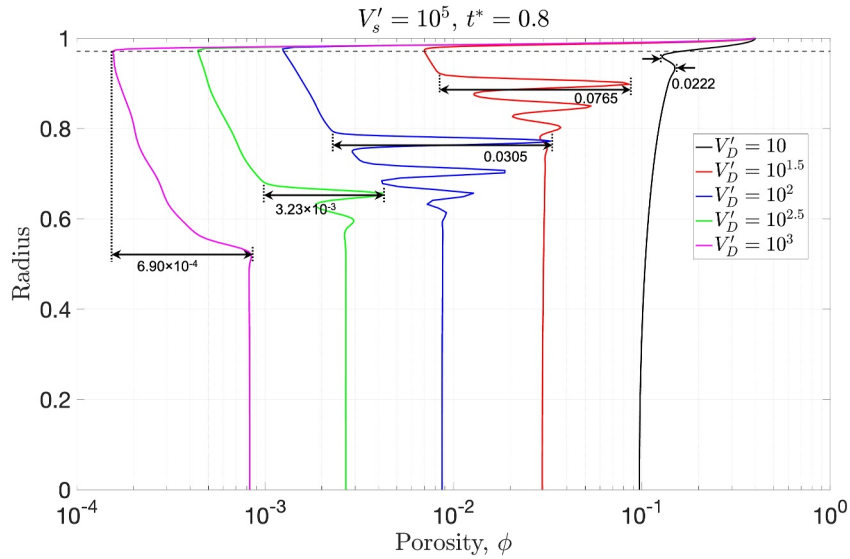

Figure 3. Porosity profiles at $V_s' = 10^5$ for different V_D' at $t^* = 0.8$, prior to the onset of instabilities. The black horizontal dashed line indicates the approximate depth of the stable boundary layer, also known as the compaction region, while the double-headed arrows show the largest porosity contrast beneath the boundary layer with approximate magnitudes indicated.

3.4. Large-Scale Instabilities

The yellow squares represent large-scale instabilities where large plume-like structures are observed (Figure 2d). They appear when $V_s' \geq 10^6$ and are associated with buoyancy instabilities at the global scale. In these simulations, $\boldsymbol{v}$ becomes the dominant mode of fluid transport within the interior and the streamlines of this velocity field are shown in Figure 2d. Similar to the second type of small-scale instabilities, the down-going plumes originate from the low porosity layer below the stable boundary layer. Hence, the plumes are expected to have widths similar to the thickness of the low porosity region. The time evolution of the 2D porosity field of Figure 2d is shown in Movie S2.

3.5. Transitionary State

Finally, a transitionary state is represented by purple diamonds. They seem to indicate the onset of large-scale instabilities even though it is not apparent from the porosity field (Figure 2e). Although the porosity structure is spherically symmetric, it shows three distinct regions: a dense solid-rich region is sandwiched between a stably stratified layer above and a liquid-rich region below. The bulk velocity streamlines show the presence of large-scale flow structures such as in Figure 2e where a degree-2 pattern is observed. However, since $|\boldsymbol{v}| < \dot{R}$, the expected rate of overturn of the interior might be rather small.

4. Discussions

4.1. From 1D to 2D Structures

The solid black line in Figure 1 indicates an approximate transition where spherically symmetric structures disappear with increasing V_s'. Although the shape of the transition can be further refined with more simulations, the envelope which the line currently traces suggests a line of symmetry at $V_D' \sim 10^{1.75}$. At $V_s' = 10^5$, this line is crossed twice with increasing V_D', corresponding to the appearance and disappearance of the small-scale instabilities, respectively. From Figure 3, two important effects are observed which are relevant to the behavior mentioned earlier with increasing V_D'. First, the high porosity layer appears further away from the stable boundary layer and second, the magnitude of the porosity difference, as indicated by the double-headed arrows, becomes smaller. At $V_D' = 10$, although the density structure below the compaction region is unstable and the porosity contrast is large, the positive buoyancy of the compaction region is sufficiently strong to inhibit the overturning of the unstable layer below. When $V_D' \geq 10^{1.5}$, the depth of the high porosity layer increases from the compaction region. Therefore, the stabilizing effect of this region is much weaker, allowing for the instabilities to grow

relatively easily as seen for $V_D' = 10^{1.5}$ and $V_D' = 10^2$. However, increasing V_D' also decreases the porosity contrast which reduces the buoyancy contrast between the layers. This eventually decreases the potential energy available to drive the instabilities and thus, small-scale instabilities do not appear at $V_D' \geq 10^{2.5}$. When V_s' is increased to $10^{5.5}$, we observe the appearance of small-scale instabilities at $V_D' = 10$ and $10^{2.5}$. This can be explained with the reduction in the overall mixture viscosity η, which subsequently allows small-scale instabilities to grow faster.

4.2. The Earth's Inner Core at Present

To understand where the Earth's inner core lies in the regime diagram today, estimates of V_s' and V_D' are needed. The physical parameter with the smallest uncertainty is R_0 as measurements from seismology has placed the inner core radius to be around 1,220 km. The other physical parameters, however, are highly uncertain. For instance, the permeability and viscosities of both solid and liquid iron alloy at pressure and temperature conditions of the inner core are highly unconstrained. The solid viscosity has been estimated to range from 10^{16} to10^{22} Pa s (Lasbleis & Deguen, 2015), while the liquid outer core viscosity is around $10^{-3} - 10^{-2}$ Pa s (Mineev & Funtikov, 2004). Moreover, estimates of the inner core age range from 0.5 to1.5 Ga (Aubert et al., 2009; Biggin et al., 2015; Bono et al., 2019; Gomi et al., 2018; Labrosse et al., 2001). In this study, we assume $\Delta\rho = 600\,\mathrm{kg\,m^{-3}}$, $g_0 = 4.4\,\mathrm{m\,s^{-2}}$, $R_0 = 1220$ km, and $t_0 = 10^9$ years (Dziewonski & Anderson, 1981; Lasbleis et al., 2020). With $\eta_s = 10^{16} - 10^{22}$ Pa s, V_s' ranges from 10^4 to10^{10}.

The value of k_0 is virtually unknown but depending on the permeability law assumed, it is possible to infer its value based on physical parameters such as grain size and tortuosity. The grain size of the inner core has been suggested to range from ∼10 cm to a few hundreds of meters (Bergman, 1998), but it is possible for much smaller grain sizes close to the ICB if the inner core is growing via the 'iron snow' mechanism (e.g., Wilczyński et al., 2023; Wong et al., 2018). Sumita et al. (1996) proposed a lower bound and upper bound for k_0 at $\sim 10^{-18}$ m^2 and $\sim 10^{-8}$ m^2 respectively. Assuming $\eta_f \sim 10^{-2}$ Pa s (Dobson et al., 2000), this puts V_D' in the range $10^{-2} - 10^8$.

The estimated ranges for V_D' and V_s' show that our simulations are within the plausible range of inner core values. Hence, it is possible for compaction-driven convection to drive large-scale flows in the inner core today, which can generate the observed large-scale seismic anisotropy.

A proxy for the expected anisotropy strength can be obtained by examining the strain rates associated with the bulk velocity field, and regions of strong deformation can produce strain-induced lattice preferred orientation of crystals. Suppose that t_a is a typical timescale for iron crystals to align its orientation relative to the deformation field. If we are to assume that the alignment is relatively instantaneous such that $t_a \ll 1/\dot{\varepsilon}_{II}$, where

$$\dot{\varepsilon}_{II} = \sqrt{\frac{1}{2}\dot{\boldsymbol{\varepsilon}}_{ij}\dot{\boldsymbol{\varepsilon}}_{ij}} \tag{15}$$

is the second invariant of the strain rate tensor $\dot{\boldsymbol{\varepsilon}}_{ij} = \frac{1}{2}\left[\nabla \boldsymbol{v} + (\nabla \boldsymbol{v})^{\dagger}\right]$, deformation textures are likely to appear today in regions where $1/\dot{\varepsilon}_{II} < t_0$. Our simulations show that anisotropy can be expected in both small- and large-scale instabilities regime. In the latter, large regions of strong deformation can appear throughout the interior (Figure S5a in Supporting Information S1), suggesting that the inner core can exhibit anisotropy on a similar scale. In the former however, we have instances of both weak (Figure S5b in Supporting Information S1) and strong (Figures S5c, S5d in Supporting Information S1) deformation signatures correlating with the instability features. Depending on the crystal structure of the iron alloy (Lincot et al., 2015), small-scale heterogeneities present in Figures S5c, S5d in Supporting Information S1 might be able to produce scattering in PKiKP coda (e.g., Leyton & Koper, 2007; Peng et al., 2008; Vidale & Earle, 2000).

In every simulation, we observe regions of stable density stratification where compaction is dominant. Apart from the unconditionally stable regime where the entire inner core is stably stratified, the other simulations show a stably stratified layer below the ICB corresponding to a boundary layer. If convective flows are present in the interior, the lower bound of $V_s' \sim 10^{4.75}$ from Figure 1 gives a maximum layer thickness of ∼5.1 km according to Equation 13. The high fluid fraction in this region can reduce seismic wave velocities and the maximum thickness obtained is within bounds of the thickness of a low velocity layer at the ICB reported from seismic studies (e.g., Attanayake et al., 2018; Tian & Wen, 2017; Zhang et al., 2023).

Lastly, ICB dynamic topography amplitudes can be estimated in the presence of instabilities (Text S7 in Supporting Information S1). Assuming that the outer core is in hydrostatic equilibrium over long timescales, the maximum peak-to-peak amplitude of ICB topography from our simulations is ~750 m (Figure S6a in Supporting Information S1). Although this might be detectable from reflected P-waves (deSilva et al., 2018), it is much smaller than the values reported by seismic studies (e.g., Dai et al., 2012; Song & Dai, 2008; Tanaka & Tkalčić, 2015). The small amplitudes might also create difficulties in differentiating between variations in topography and mushy layer thickness. Nevertheless, ICB topography can potentially play an important role in outer core dynamics similar to CMB topography effects on the flow and geodynamo (Calkins et al., 2012; Mandea et al., 2015; Wu & Roberts, 2013), while the topography wavelength might provide constrains on dynamic processes in the inner core's interior (Figure S6b in Supporting Information S1). An interesting consequence of density variations from these large-scale flows is the potential effects on Earth's length-of-day variations through gravitational coupling between the mantle and inner core (e.g., Davies et al., 2014; Roberts & Aurnou, 2012).

5. Conclusion

We have modeled the dynamics of inner core growth through the compaction of a mush using the two-phase formulation, with the porosity structure determined by two dimensionless parameters: V'_D and V'_s. Our simulations in an axisymmetric spherical geometry have shown that for $V'_s \geq 10^5$, compaction-driven convection can occur when $10 \leq V'_D \leq 10^{2.5}$. While this study provides an understanding of inner core convection arising from compaction and fluid migration, future work should include thermal, compositional, phase change, and rheological effects as these might be important in inner core dynamics. Although our strain rate estimates suggest that compaction-driven convection can produce significant texturing, we do not produce the N-S inner core anisotropy. Additional ingredients needed to organize the convective motion and make it approximately axisymmetric around the N-S axis include: the effects of the Lorentz forces (Karato, 1999) and heterogeneous growth of the inner core caused by CMB heat flux variations (Aubert et al., 2008; Sreenivasan & Gubbins, 2011; Sumita & Olson, 1999) on the orientation of convective motions. These will be investigated in future studies.

Data Availability Statement

Supporting Information includes Texts S1-S7, Figures S1–S7 in Supporting Information S1, and Movie captions Movie S1 and Movie S2. The data files used in this paper are available at (Lim et al., 2024).

Acknowledgments
The authors wish to thank Marine Lasbleis, Stéphane Labrosse, John Hernlund, and Paolo Personnettaz for discussions. We also thank Michael Bergman and Ikuro Sumita for their insightful comments which helped improve our manuscript, and editor Quentin Williams for handling the manuscript. Authors KWL and MM received funding from the European Research Council (ERC) under the European Union Horizon 2020 research and innovation programme via GRACEFUL Synergy Grant 855677. DC received funding from the ERC under the European Union's Horizon 2020 research and innovation programme via the THEIA project (grant agreement no. 847433). ISTerre is part of Labex OSUG@2020 (ANR10 LABX56). The computations have been performed on the local cluster of ISTerre. DC acknowledges support from GRICAD infrastructure (https://gricad.univ-grenoble-alpes.fr), and HPC resources (Jean Zay V100) of IDRIS under allocation AD010413621 attributed by GENCI (Grand Equipement National de Calcul Intensif).

References

Aharonov, E., Whitehead, J., Kelemen, P., & Spiegelman, M. (1995). Channeling instability of upwelling melt in the mantle. *Journal of Geophysical Research*, *100*(B10), 20433–20450. https://doi.org/10.1029/95jb01307

Alexandrov, D., & Malygin, A. (2011). Coupled convective and morphological instability of the inner core boundary of the Earth. *Physics of the Earth and Planetary Interiors*, *189*(3–4), 134–141. https://doi.org/10.1016/j.pepi.2011.08.004

Andrews, J., Deuss, A., & Woodhouse, J. (2006). Coupled normal-mode sensitivity to inner-core shear velocity and attenuation. *Geophysical Journal International*, *167*(1), 204–212. https://doi.org/10.1111/j.1365-246x.2006.03022.x

Attanayake, J., Thomas, C., Cormier, V. F., Miller, M. S., & Koper, K. D. (2018). Irregular transition layer beneath the Earth's inner core boundary from observations of antipodal PKIKP and PKIIKP waves. *Geochemistry, Geophysics, Geosystems*, *19*(10), 3607–3622. https://doi.org/10.1029/2018gc007562

Aubert, J., Amit, H., Hulot, G., & Olson, P. (2008). Thermochemical flows couple the Earth's inner core growth to mantle heterogeneity. *Nature*, *454*(7205), 758–761. https://doi.org/10.1038/nature07109

Aubert, J., Labrosse, S., & Poitou, C. (2009). Modelling the palaeo-evolution of the geodynamo. *Geophysical Journal International*, *179*(3), 1414–1428. https://doi.org/10.1111/j.1365-246x.2009.04361.x

Bercovici, D., Ricard, Y., & Schubert, G. (2001). A two-phase model for compaction and damage: 1. General theory. *Journal of Geophysical Research*, *106*(B5), 8887–8906. https://doi.org/10.1029/2000jb900430

Bergman, M. I. (1998). Estimates of the Earth's inner core grain size. *Geophysical Research Letters*, *25*(10), 1593–1596. https://doi.org/10.1029/98gl01239

Biggin, A. J., Piispa, E., Pesonen, L. J., Holme, R., Paterson, G., Veikkolainen, T., & Tauxe, L. (2015). Palaeomagnetic field intensity variations suggest Mesoproterozoic inner-core nucleation. *Nature*, *526*(7572), 245–248. https://doi.org/10.1038/nature15523

Bono, R. K., Tarduno, J. A., Nimmo, F., & Cottrell, R. D. (2019). Young inner core inferred from Ediacaran ultra-low geomagnetic field intensity. *Nature Geoscience*, *12*(2), 143–147. https://doi.org/10.1038/s41561-018-0288-0

Boukaré, C.-E., & Ricard, Y. (2017). Modeling phase separation and phase change for magma ocean solidification dynamics. *Geochemistry, Geophysics, Geosystems*, *18*(9), 3385–3404. https://doi.org/10.1002/2017gc006902

Breuer, D., Rueckriemen, T., & Spohn, T. (2015). Iron snow, crystal floats, and inner-core growth: Modes of core solidification and implications for dynamos in terrestrial planets and moons. *Progress in Earth and Planetary Science*, *2*, 1–26. https://doi.org/10.1186/s40645-015-0069-y

Buffett, B. (2015). 8.08 - core–mantle interactions. In G. Schubert (Ed.), *Treatise on Geophysics* (2nd ed., pp. 213–224). Elsevier. https://doi.org/10.1016/B978-0-444-53802-4.00148-2

Calkins, M. A., Noir, J., Eldredge, J. D., & Aurnou, J. M. (2012). The effects of boundary topography on convection in Earth's core. *Geophysical Journal International*, *189*(2), 799–814. https://doi.org/10.1111/j.1365-246x.2012.05415.x

Cao, A., & Romanowicz, B. (2009). Constraints on shear wave attenuation in the Earth's inner core from an observation of PKJKP. *Geophysical Research Letters*, *36*(9). https://doi.org/10.1029/2009gl038342

Dai, Z., Wang, W., & Wen, L. (2012). Irregular topography at the Earth's inner core boundary. *Proceedings of the National Academy of Sciences*, *109*(20), 7654–7658. https://doi.org/10.1073/pnas.1116342109

Davies, C. J., Stegman, D. R., & Dumberry, M. (2014). The strength of gravitational core-mantle coupling. *Geophysical Research Letters*, *41*(11), 3786–3792. https://doi.org/10.1002/2014gl059836

Deguen, R., Alboussière, T., & Brito, D. (2007). On the existence and structure of a mush at the inner core boundary of the Earth. *Physics of the Earth and Planetary Interiors*, *164*(1–2), 36–49. https://doi.org/10.1016/j.pepi.2007.05.003

Deguen, R., & Cardin, P. (2011). Thermochemical convection in Earth's inner core. *Geophysical Journal International*, *187*(3), 1101–1118. https://doi.org/10.1111/j.1365-246x.2011.05222.x

Deuss, A. (2014). Heterogeneity and anisotropy of Earth's inner core. *Annual Review of Earth and Planetary Sciences*, *42*(1), 103–126. https://doi.org/10.1146/annurev-earth-060313-054658

deSilva, S., Cormier, V. F., & Zheng, Y. (2018). Inner core boundary topography explored with reflected and diffracted P waves. *Physics of the Earth and Planetary Interiors*, *276*, 202–214. https://doi.org/10.1016/j.pepi.2017.04.008

Dobson, D. P., Crichton, W. A., Vočadlo, L., Jones, A. P., Wang, Y., Uchida, T., et al. (2000). In situ measurement of viscosity of liquids in the Fe-FeS system at high pressures and temperatures. *American Mineralogist*, *85*(11–12), 1838–1842. https://doi.org/10.2138/am-2000-11-1231

Driscoll, P. E. (2016). Simulating 2 Ga of geodynamo history. *Geophysical Research Letters*, *43*(11), 5680–5687. https://doi.org/10.1002/2016gl068858

Dziewonski, A. M., & Anderson, D. L. (1981). Preliminary reference Earth model. *Physics of theEearth and Planetary Interiors*, *25*(4), 297–356. https://doi.org/10.1016/0031-9201(81)90046-7

Faul, U. H. (2001). Melt retention and segregation beneath mid-ocean ridges. *Nature*, *410*(6831), 920–923. https://doi.org/10.1038/35073556

Fearn, D. R., Loper, D. E., & Roberts, P. H. (1981). Structure of the Earth's inner core. *Nature*, *292*(5820), 232–233. https://doi.org/10.1038/292232a0

Gomi, H., Fei, Y., & Yoshino, T. (2018). The effects of ferromagnetism and interstitial hydrogen on the equation of states of hcp and dhcp FeHx: Implications for the Earth's inner core age. *American Mineralogist*, *103*(8), 1271–1281. https://doi.org/10.2138/am-2018-6295

Gubbins, D., Masters, G., & Nimmo, F. (2008). A thermochemical boundary layer at the base of Earth's outer core and independent estimate of core heat flux. *Geophysical Journal International*, *174*(3), 1007–1018. https://doi.org/10.1111/j.1365-246x.2008.03879.x

Hernlund, J., & McNamara, A. (2015). 7.11 - the core–mantle boundary region. In G. Schubert (Ed.), *Treatise on Geophysics* (Second Edition ed., pp. 461–519). Elsevier. https://doi.org/10.1016/B978-0-444-53802-4.00136-6

Hier-Majumder, S., Ricard, Y., & Bercovici, D. (2006). Role of grain boundaries in magma migration and storage. *Earth and Planetary Science Letters*, *248*(3–4), 735–749. https://doi.org/10.1016/j.epsl.2006.06.015

Hirose, K., Labrosse, S., & Hernlund, J. (2013). Composition and state of the core. *Annual Review of Earth and Planetary Sciences*, *41*(1), 657–691. https://doi.org/10.1146/annurev-earth-050212-124007

Huguet, L., Van Orman, J. A., Hauck, S. A., & Willard, M. A. (2018). Earth's inner core nucleation paradox. *Earth and Planetary Science Letters*, *487*, 9–20. https://doi.org/10.1016/j.epsl.2018.01.018

Karato, S.-i. (1999). Seismic anisotropy of the Earth's inner core resulting from flow induced by Maxwell stresses. *Nature*, *402*(6764), 871–873. https://doi.org/10.1038/47235

Labrosse, S. (2015). Thermal evolution of the core with a high thermal conductivity. *Physics of the Earth and Planetary Interiors*, *247*, 36–55. https://doi.org/10.1016/j.pepi.2015.02.002

Labrosse, S., Poirier, J.-P., & Le Mouël, J.-L. (2001). The age of the inner core. *Earth and Planetary Science Letters*, *190*(3–4), 111–123. https://doi.org/10.1016/s0012-821x(01)00387-9

Landeau, M., Aubert, J., & Olson, P. (2017). The signature of inner-core nucleation on the geodynamo. *Earth and Planetary Science Letters*, *465*, 193–204. https://doi.org/10.1016/j.epsl.2017.02.004

Lasbleis, M., & Deguen, R. (2015). Building a regime diagram for the Earth's inner core. *Physics of the Earth and Planetary Interiors*, *247*, 80–93. https://doi.org/10.1016/j.pepi.2015.02.001

Lasbleis, M., Kervazo, M., & Choblet, G. (2020). The fate of liquids trapped during the Earth's inner core growth. *Geophysical Research Letters*, *47*(2), e2019GL085654. https://doi.org/10.1029/2019gl085654

Lee, C., Cerpa, N. G., Han, D., & Wada, I. (2024). Modeling liquid transport in the Earth's mantle as two-phase flow: Effect of an enforced positive porosity on liquid flow and mass conservation. *Solid Earth*, *15*(1), 23–38. https://doi.org/10.5194/se-15-23-2024

Leyton, F., & Koper, K. D. (2007). Using PKiKP coda to determine inner core structure: 1. Synthesis of coda envelopes using single-scattering theories. *Journal of Geophysical Research*, *112*(B5). https://doi.org/10.1029/2006jb004369

Lim, K. W., Deguen, R., Cébron, D., Schulze, A., & Mandea, M. (2024). Data availability for "Compaction-driven convection in the growing inner core" (Version v2) [Dataset]. *Zenodo*. https://doi.org/10.5281/zenodo.14000753

Lincot, A., Merkel, S., & Cardin, P. (2015). Is inner core seismic anisotropy a marker for plastic flow of cubic iron? *Geophysical Research Letters*, *42*(5), 1326–1333. https://doi.org/10.1002/2014gl062862

Loper, D. E., & Fearn, D. R. (1983). A seismic model of a partially molten inner core. *Journal of Geophysical Research*, *88*(B2), 1235–1242. https://doi.org/10.1029/jb088ib02p01235

Loper, D. E., & Roberts, P. H. (1981). A study of conditions at the inner core boundary of the Earth. *Physics of the Earth and Planetary Interiors*, *24*(4), 302–307. https://doi.org/10.1016/0031-9201(81)90117-5

Mandea, M., Narteau, C., Panet, I., & Le Mouël, J.-L. (2015). Gravimetric and magnetic anomalies produced by dissolution-crystallization at the core-mantle boundary. *Journal of Geophysical Research: Solid Earth*, *120*(9), 5983–6000. https://doi.org/10.1002/2015jb012048

McDonough, W. (2014). 3.16 - Compositional Model for the Earth's Core. In H. D. Holland & K. K. Turekian (Eds.), *Treatise on Geochemistry* (pp. 559–577). Elsevier. https://doi.org/10.1016/B978-0-08-095975-7.00215-1

McKenzie, D. (1984). The generation and compaction of partially molten rock. *Journal of Petrology*, *25*(3), 713–765. https://doi.org/10.1093/petrology/25.3.713

Mineev, V. N., & Funtikov, A. I. (2004). Viscosity measurements on metal melts at high pressure and viscosity calculations for the Earth's core. *Physics-Uspekhi*, *47*(7), 671–686. https://doi.org/10.1070/pu2004v047n07abeh001746

Morelli, A., Dziewonski, A. M., & Woodhouse, J. H. (1986). Anisotropy of the inner core inferred from PKIKP travel times. *Geophysical Research Letters*, *13*(13), 1545–1548. https://doi.org/10.1029/gl013i013p01545

Peng, Z., Koper, K. D., Vidale, J. E., Leyton, F., & Shearer, P. (2008). Inner-core fine-scale structure from scattered waves recorded by LASA. *Journal of Geophysical Research*, *113*(B9). https://doi.org/10.1029/2007jb005412

Poupinet, G., Pillet, R., & Souriau, A. (1983). Possible heterogeneity of the Earth's core deduced from PKIKP travel times. *Nature*, *305*(5931), 204–206. https://doi.org/10.1038/305204a0

Roberts, P. H., & Aurnou, J. M. (2012). On the theory of core-mantle coupling. *Geophysical and Astrophysical Fluid Dynamics*, *106*(2), 157–230. https://doi.org/10.1080/03091929.2011.589028

Scott, D. R., & Stevenson, D. J. (1986). Magma ascent by porous flow. *Journal of Geophysical Research*, *91*(B9), 9283–9296. https://doi.org/10.1029/jb091ib09p09283

Shcherbakova, V., Bakhmutov, V., Thallner, D., Shcherbakov, V., Zhidkov, G., & Biggin, A. (2020). Ultra-low palaeointensities from East European Craton, Ukraine support a globally anomalous palaeomagnetic field in the Ediacaran. *Geophysical Journal International*, *220*(3), 1928–1946. https://doi.org/10.1093/gji/ggz566

Shimizu, H., Poirier, J., & Le Mouël, J. (2005). On crystallization at the inner core boundary. *Physics of the Earth and Planetary Interiors*, *151*(1–2), 37–51. https://doi.org/10.1016/j.pepi.2005.01.001

Singh, S., Taylor, M., & Montagner, J. (2000). On the presence of liquid in Earth's inner core. *Science*, *287*(5462), 2471–2474. https://doi.org/10.1126/science.287.5462.2471

Song, X., & Dai, W. (2008). Topography of Earth's inner core boundary from high-quality waveform doublets. *Geophysical Journal International*, *175*(1), 386–399. https://doi.org/10.1111/j.1365-246x.2008.03909.x

Song, X., & Helmberger, D. V. (1993). Anisotropy of Earth's inner core. *Geophysical Research Letters*, *20*(23), 2591–2594. https://doi.org/10.1029/93gl02812

Souriau, A., & Calvet, M. (2015). 1.23 - Deep Earth Structure: The Earth's Cores. In G. Schubert (Ed.), *Treatise on Geophysics* (2nd ed., pp. 725–757). Elsevier. https://doi.org/10.1016/B978-0-444-53802-4.00020-8

Sreenivasan, B., & Gubbins, D. (2011). On mantle-induced heat flow variations at the inner core boundary. *Physics of the Earth and Planetary Interiors*, *187*(3–4), 336–341. https://doi.org/10.1016/j.pepi.2011.06.006

Sumita, I., & Bergman, M. (2015). 8.12 - Inner Core Dynamics. In G. Schubert (Ed.), *Treatise on Geophysics* (2nd ed., pp. 297–316). Elsevier. https://doi.org/10.1016/B978-0-444-53802-4.00143-3

Sumita, I., & Olson, P. (1999). A laboratory model for convection in Earth's core driven by a thermally heterogeneous mantle. *Science*, *286*(5444), 1547–1549. https://doi.org/10.1126/science.286.5444.1547

Sumita, I., Yoshida, S., Kumazawa, M., & Hamano, Y. (1996). A model for sedimentary compaction of a viscous medium and its application to inner-core growth. *Geophysical Journal International*, *124*(2), 502–524. https://doi.org/10.1111/j.1365-246x.1996.tb07034.x

Tanaka, S., & Tkalčić, H. (2015). Complex inner core boundary from frequency characteristics of the reflection coefficients of PKiKP waves observed by Hi-net. *Progress in Earth and Planetary Science*, *2*, 1–16. https://doi.org/10.1186/s40645-015-0064-3

Thallner, D., Biggin, A. J., & Halls, H. C. (2021). An extended period of extremely weak geomagnetic field suggested by palaeointensities from the Ediacaran Grenville dykes (SE Canada). *Earth and Planetary Science Letters*, *568*, 117025. https://doi.org/10.1016/j.epsl.2021.117025

Tian, D., & Wen, L. (2017). Seismological evidence for a localized mushy zone at the Earth's inner core boundary. *Nature Communications*, *8*(1), 165. https://doi.org/10.1038/s41467-017-00229-9

Tkalčić, H., & Phạm, T.-S. (2018). Shear properties of Earth's inner core constrained by a detection of J waves in global correlation wavefield. *Science*, *362*(6412), 329–332. https://doi.org/10.1126/science.aau7649

Tkalčić, H., Wang, S., & Phạm, T.-S. (2022). Shear properties of Earth's inner core. *Annual Review of Earth and Planetary Sciences*, *50*(1), 153–181. https://doi.org/10.1146/annurev-earth-071521-063942

Turcotte, D. L., & Morgan, J. P. (1992). The physics of magma migration and mantle flow beneath a mid-ocean ridge. *Geophysical Monograph Series*, *71*, 155–182. https://doi.org/10.1029/gm071p0155

Vidale, J. E., & Earle, P. S. (2000). Fine-scale heterogeneity in the Earth's inner core. *Nature*, *404*(6775), 273–275. https://doi.org/10.1038/35005059

Vočadlo, L. (2007). Ab initio calculations of the elasticity of iron and iron alloys at inner core conditions: Evidence for a partially molten inner core? *Earth and Planetary Science Letters*, *254*(1–2), 227–232. https://doi.org/10.1016/j.epsl.2006.09.046

von Bargen, N., & Waff, H. S. (1986). Permeabilities, interfacial areas and curvatures of partially molten systems: Results of numerical computations of equilibrium microstructures. *Journal of Geophysical Research*, *91*(B9), 9261–9276. https://doi.org/10.1029/jb091ib09p09261

Waszek, L., Irving, J., Phạm, T.-S., & Tkalčić, H. (2023). Seismic insights into Earth's core. *Nature Communications*, *14*(1), 6029. https://doi.org/10.1038/s41467-023-41725-5

Wilczyński, F., Davies, C. J., & Jones, C. A. (2023). A two-phase pure slurry model for planetary cores: One-dimensional solutions and implications for Earth's F-layer. *Journal of Fluid Mechanics*, *976*, A5. https://doi.org/10.1017/jfm.2023.834

Wilson, A. J., Walker, A. M., Alfè, D., & Davies, C. J. (2021). Probing the nucleation of iron in Earth's core using molecular dynamics simulations of supercooled liquids. *Physical Review B*, *103*(21), 214113. https://doi.org/10.1103/physrevb.103.214113

Wong, J., Davies, C. J., & Jones, C. A. (2018). A Boussinesq slurry model of the F-layer at the base of Earth's outer core. *Geophysical Journal International*, *214*(3), 2236–2249. https://doi.org/10.1093/gji/ggy245

Wong, J., Davies, C. J., & Jones, C. A. (2021). A regime diagram for the slurry F-layer at the base of Earth's outer core. *Earth and Planetary Science Letters*, *560*, 116791. https://doi.org/10.1016/j.epsl.2021.116791

Woodhouse, J. H., Giardini, D., & Li, X.-D. (1986). Evidence for inner core anisotropy from free oscillations. *Geophysical Research Letters*, *13*(13), 1549–1552. https://doi.org/10.1029/gl013i013p01549

Wu, C.-C., & Roberts, P. H. (2013). On a dynamo driven topographically by longitudinal libration. *Geophysical and Astrophysical Fluid Dynamics*, *107*(1–2), 20–44. https://doi.org/10.1080/03091929.2012.682990

Zhang, B., Ni, S., Wu, W., Shen, Z., Wang, W., Sun, D., & Wu, Z. (2023). Small-scale layered structures at the inner core boundary. *Nature Communications*, *14*(1), 6362. https://doi.org/10.1038/s41467-023-42177-7

References From the Supporting Information

Barcilon, V., & Richter, F. M. (1986). Nonlinear waves in compacting media. *Journal of Fluid Mechanics*, *164*, 429–448. https://doi.org/10.1017/s0022112086002628

Gresho, P. M., & Lee, R. L. (1981). Don't suppress the wiggles—They're telling you something. *Computers & Fluids*, *9*(2), 223–253. https://doi.org/10.1016/0045-7930(81)90026-8

Hernlund, J. W., & Jellinek, A. M. (2010). Dynamics and structure of a stirred partially molten ultralow-velocity zone. *Earth and Planetary Science Letters*, *296*(1–2), 1–8. https://doi.org/10.1016/j.epsl.2010.04.027

Johnson, C., Navert, U., & Pitkaranta, J. (1984). Finite element methods for linear hyperbolic problems. *Computer Methods in Applied Mechanics and Engineering*, *45*(1–3), 285–312. https://doi.org/10.1016/0045-7825(84)90158-0

Olson, P., & Christensen, U. (1986). Solitary wave propagation in a fluid conduit within a viscous matrix. *Journal of Geophysical Research*, *91*(B6), 6367–6374. https://doi.org/10.1029/jb091ib06p06367

Schaeffer, N. (2013). Efficient spherical harmonic transforms aimed at pseudospectral numerical simulations. *Geochemistry, Geophysics, Geosystems*, *14*(3), 751–758. https://doi.org/10.1002/ggge.20071

Scott, D. R., Stevenson, D. J., & Whitehead, J. A., Jr. (1986). Observations of solitary waves in a viscously deformable pipe. *Nature*, *319*(6056), 759–761. https://doi.org/10.1038/319759a0

Spiegelman, M. (1993). Flow in deformable porous media. Part 2 numerical analysis–the relationship between shock waves and solitary waves. *Journal of Fluid Mechanics*, *247*, 39–63. https://doi.org/10.1017/s0022112093000370

Šrámek, O., Ricard, Y., & Bercovici, D. (2007). Simultaneous melting and compaction in deformable two-phase media. *Geophysical Journal International*, *168*(3), 964–982. https://doi.org/10.1111/j.1365-246x.2006.03269.x

Yarushina, V. M., Podladchikov, Y. Y., & Connolly, J. A. (2015). (De) compaction of porous viscoelastoplastic media: Solitary porosity waves. *Journal of Geophysical Research: Solid Earth*, *120*(7), 4843–4862. https://doi.org/10.1002/2014jb011260